

# Lawrence Berkeley National Laboratory

## Climate & Ecosystems

### Title

Continuous increase in evaporative demand shortened the growing season of European ecosystems in the last decade

### Permalink

<https://escholarship.org/uc/item/7cq738qf>

### Journal

Communications Earth & Environment, 4(1)

### ISSN

2662-4435

### Authors

Rahmati, Mehdi  
Graf, Alexander  
Poppe Terán, Christian  
et al.

### Publication Date

2023

### DOI












10.1038/s43247-023-00890-7

### Copyright Information

This work is made available under the terms of a Creative Commons Attribution-NonCommercial-NoDerivatives License, available at <https://creativecommons.org/licenses/by-nc-nd/4.0/>

Peer reviewed

## Continuous increase in evaporative demand shortened the growing season of European ecosystems in the last decade

Mehdi Rahmati <sup>1,2✉</sup>, Alexander Graf <sup>2</sup>, Christian Poppe Terán <sup>2</sup>, Wulf Amelung<sup>3</sup>, Wouter Dorigo <sup>4</sup>, Harrie-Jan Hendricks Franssen <sup>2</sup>, Carsten Montzka <sup>2</sup>, Dani Or <sup>5,6</sup>, Matthias Sprenger <sup>7</sup>, Jan Vanderborght <sup>2</sup>, Niko E. C. Verhoest <sup>8</sup> & Harry Vereecken <sup>2✉</sup>

Despite previous reports on European growing seasons lengthening due to global warming, evidence shows that this trend has been reversing in the past decade due to increased transpiration needs. To assess this, we used an innovative method along with space-based observations to determine the timing of greening and dormancy and then to determine existing trends of them and causes. Early greening still occurs, albeit at slower rates than before. However, a recent (2011–2020) shift in the timing of dormancy has caused the season length to decrease back to 1980s levels. This shortening of season length is attributed primarily to higher atmospheric water demand in summer that suppresses transpiration even for soil moisture levels as of previous years. Transpiration suppression implies that vegetation is unable to meet the high transpiration needs. Our results have implications for future management of European ecosystems (e.g., net carbon balance and water and energy exchange with atmosphere) in a warmer world.

<sup>1</sup>Department of Soil Science and Engineering, University of Maragheh, Maragheh, Iran. <sup>2</sup>Agrosphere Institute, IBG-3, Forschungszentrum Jülich GmbH, 52425 Jülich, Germany. <sup>3</sup>Institute of Crop Science and Resource Conservation (INRES)- Soil Science and Soil Ecology, University of Bonn, Bonn, Germany. <sup>4</sup>Department of Geodesy and Geoinformation, TU Wien, Vienna, Austria. <sup>5</sup>Department of Environmental Systems Science, ETH Zurich, Zurich, Switzerland. <sup>6</sup>Division of Hydrologic Sciences (DHS) - Desert Research Institute, Reno, NV, USA. <sup>7</sup>Lawrence Berkeley National Laboratory, Berkeley, CA, USA. <sup>8</sup>Hydro-Climate Extremes Lab, Ghent University, Ghent, Belgium. ✉email: [mehdirmti@gmail.com](mailto:mehdirmti@gmail.com); [h.vereecken@fz-juelich.de](mailto:h.vereecken@fz-juelich.de)

Vegetation phenology is a sensitive indicator of changes in climatic conditions<sup>1–5</sup>. The timing of the onset of greening (OG) in spring<sup>6–8</sup> and the onset of dormancy (OD) in the autumn (See the Supplementary Note on phenological stages of different vegetation types) are among the most important phenological events marking the growing season length (GSL) in mid- and high- latitudes<sup>9–11</sup>. Global warming, particularly in the Northern Hemisphere, has led to an earlier onset of the vegetation cycle, as evidenced by both ground measurements<sup>9,12–14</sup> and satellite-based monitoring of land surface greenness<sup>15,16</sup>. Although the results for early OG are in good agreement, conflicting assessments have been made when evaluating the impact of global warming on the timing of OD, with some reporting delayed OD<sup>7,17,18</sup> and others reporting earlier OD<sup>19,20</sup>. Delayed OD is most likely due to increased photosynthetic enzyme activity<sup>21</sup>, decreased chlorophyll degradation rate<sup>22</sup>, decreased likelihood of exposure to frost in the autumn<sup>23,24</sup>, or increased capacity for growth and photosynthetic consumption, all caused by increased temperature (T)<sup>17</sup>. In many cases, earlier dormancy is due to limited leaf life<sup>19</sup> or lower plant productivity later in the season due to water deficits<sup>20</sup>. A schematic putative explanation for climate change and soil moisture (SM) changes during the growing season (GS) and their effects on OG and OD is provided in Fig. 1.

Observations in the northern hemisphere<sup>25</sup> show that during 1982–2011, earlier OG and increased evapotranspiration (ET) in spring have contributed to an additional deficit in SM in summer, which can induce an earlier OD. However, the impact of a summer SM deficit on OD due to increasing ET requires analyses of long-term relationships between ET, SM and OD. We recognize that ET alone does not determine SM and OD, but precipitation (P) is an important factor, simply because reduced P for constant ET will also result in lower SM and possibly induce earlier dormancy. To complicate matters further, we need to consider the possibility that neither P nor SM affect GSL but increased atmospheric water demand (AWD), or increased vapor pressure deficit (VPD) as a measure of AWD, can disrupt the soil-plant-atmosphere water continuum by regulating early stomatal closure and OD. This may be accompanied by increased ET, but not always as a simultaneous increase in AWD and partial closure of the stomata may result in no change in ET. Therefore, it is important to investigate whether reduced SM leads to earlier OD or whether increased AWD becomes limiting for certain vegetation types even with constant SM levels. To address these questions, we need to consider seasonal variations in VPD and SM as well as their interactions with OG and OD and some meteorological variables such as P, T, and ET.

Considering the foregoing discussion, several mechanisms can affect the OD, including 1) low T, 2) water deficiency (caused by increased ET or decreased P, or a combination of both),

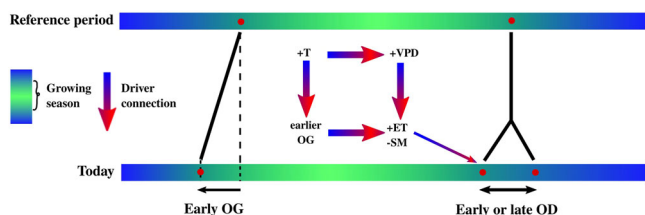


**Fig. 1** Schematic representation of the effects of climate change on the occurrence of onset of greening (OG) and dormancy (OD) that determine growing season length (GSL). It shows the effect of increased temperature (T) in spring on early OG and the effect of increased T in summer on increased vapor pressure deficit (VPD) and decreased soil moisture (SM) and consequently on OD.

3) maximum leaf age (earlier OG leads to earlier OD), and 4) other plant stressors (heat stress or breakdown of xylem capillaries due to high AWD). Climate change can affect all four of these causes, and some may act in opposite directions. For example, higher T in fall may delay OD, while an increase in P deficit may result in earlier OD.

Therefore, the objectives of our analysis were to study 1) whether existing data support the hypothesis of consistent previous shifts in OG, OD, and consequently GSL in Europe for the period 1982 to 2020, 2) can meteorological variables along with SM data explain possible shifts, and finally 3) elucidate the different roles of water and energy supply as drivers for GSL changes.

## Results and discussion

The spatial variation of the long-term (1982–2020) mean GSL for Europe derived from OD and OG data is depicted in Fig. 2 (see Supplementary Fig. 1 for spatial variations of OG and OD). We also present trends in OG and OD over time across Europe in Fig. 3. These results were obtained from application of innovative LFD-NDVI method (see details in Methods) to long-term (1982–2015) GIMMS<sup>26,27</sup> NDVI data augmented by AVHRR<sup>28</sup> (1982–2017) and MODIS<sup>29</sup> (2001–2020) NDVI data (see Supplementary Discussion 1 on the use of space-based observation in deriving phenological data). These were followed by application of the Mann-Kendall test<sup>30,31</sup> (see Methods) to examine the significance of the trends in GSL, OG, and OD data from 1982 to 2020. Our analysis confirms reports of early greening in Europe<sup>11,32</sup> showing a significant trend towards earlier greening in 35% of the pixels (see Supplementary Fig. 2a), with OG shifting from mid-April during 1982–1990 to early April in the latter period (2011–2020), resulting in an average of 11 days earlier greening in these pixels. For 63% of the pixels, we detected no significant trend despite a small shift of up to 3 days earlier OG. Only 2% of pixels show a significant trend toward delayed OG, with OG shifting by 16 days on average from early April in 1982–1990 to mid-April in 2011–2020. The amplitude of the shift (3–11 days per total period, equivalent to ~1–3 days per decade) is within the range of values reported by other researchers<sup>8,25,33</sup> reporting an earlier OG from ~1 to ~5 days per decade.

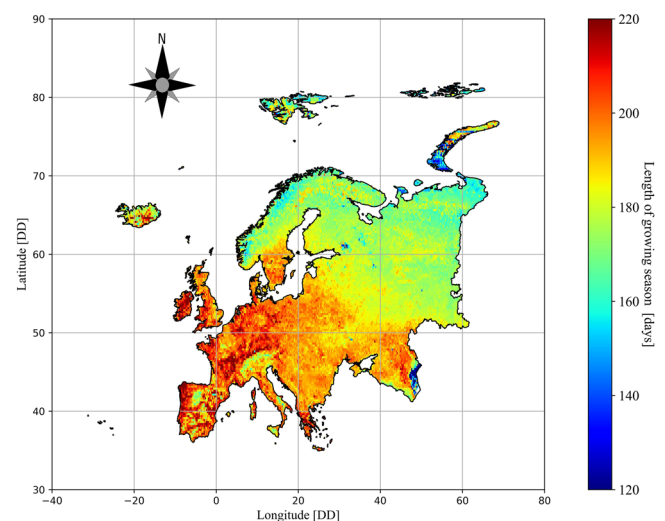


**Fig. 2** Spatial variation of the long-term (1982–2020) average growing season length (GSL) in Europe. Overall, the growing season in Europe is longer at lower latitudes, reaching about 220 days, and shorter at higher latitudes, reaching about 120 days. DD stands for decimal degree.

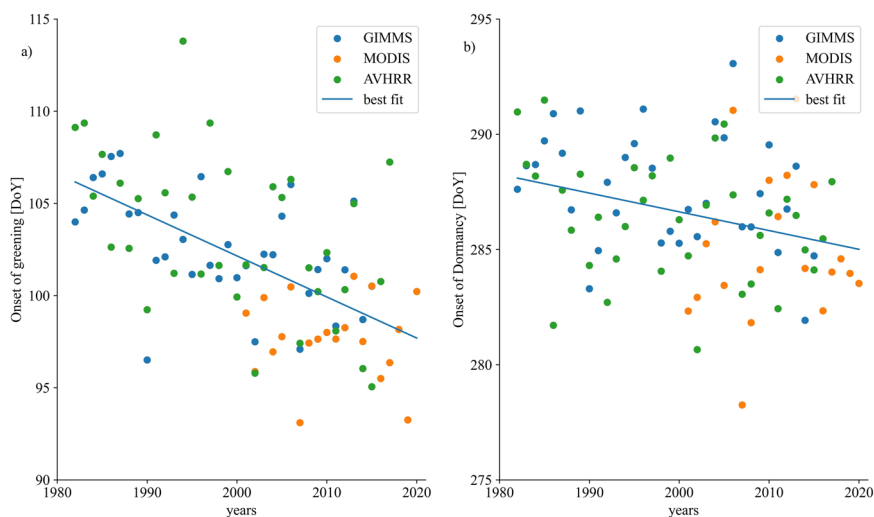


**Fig. 3 Temporal variations (1982–2020) of the beginning and end of the growing season in Europe.** Panel **a** shows the average onset of greening and panel **b** the average onset of dormancy. The onsets of greening and dormancy are derived from different remote sensing data products.

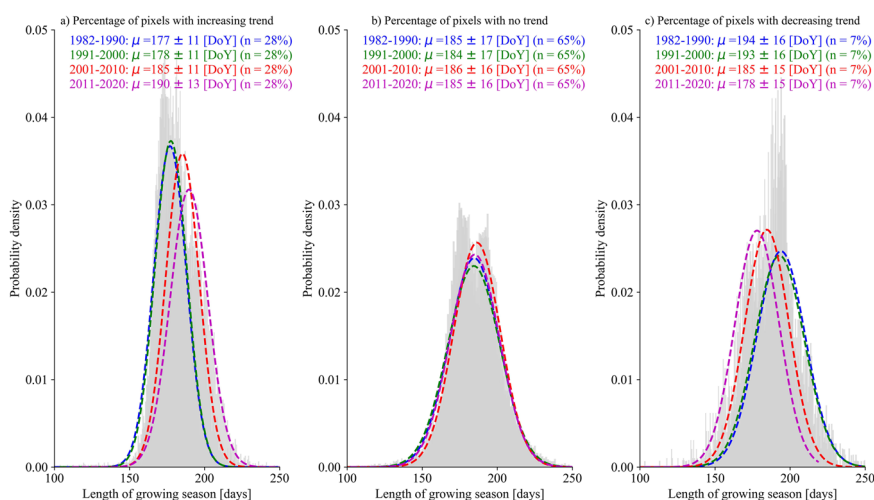


**Fig. 4 Histograms and probability distribution functions (PDFs) of the length of the growing season in different decades.** Panel **a** shows the histograms (grey bars) and PDFs (dashed lines) for pixels with increasing trend, panel **b** for pixels with decreasing trend and panel **c** for pixels without significant trend. The letter  $\mu$  corresponds to the mean  $\pm$  standard deviations and  $n$  corresponds to the percentage of pixels in each group.

Results indicate that OD has a more complicated response to climate warming than OG with 73% of the pixels showing no significant trend in OD (see Supplementary Fig. 2b) where OD occurs around October 13 ( $\pm 1$  day). For 17% of the pixels OD occurred earlier, shifting from mid-October in 1982–1990 to early October in 2011–2020, while the opposite trend (shifting to later days) is observed over 10% of pixels only. In contrast to our results, Liu et al.<sup>17</sup> using the same GIMMS NDVI data, observed a trend toward later OD at  $\sim 70\%$  of Northern Hemisphere pixels between 1982 and 2011 (at a mean rate of  $0.18 \pm 0.38$  d/y). Other studies, e.g., Julien and Sobrino<sup>33</sup>, also using the same GIMMS NDVI data and examining the period 1981–2003, show a later OD, but on a global scale.

Finally, almost two-thirds of the pixels (65%) showed no significant trend in GSL (Fig. 4), as the GSL remains constant at 185 days ( $\pm 1$  day). For 28% of the pixels GSL exhibited a lengthening trend with nearly 13 days on average from 177 to 190 days. For 7% of the pixels, we observed shortening of the GSL by 16 days on average from 194 to 178 days. Julien and Sobrino<sup>33</sup> have used similar GIMMS NDVI data considering a shorter period from 1981 to 2003. In their analysis GSL increased by 0.8

d/y worldwide. Similarly, Stöckli and Vidale<sup>34</sup> found an increase of 0.96 d/y for Europe during the 1982–2001 period. Other researchers<sup>15,35,36</sup> also report increasing GSL in the Northern Hemisphere in earlier decades (before 2010). For our longer period (1982–2020) and Europe, the average increase is only one third of the reported values ( $\sim 0.3$  d/y), and a lengthening occurs in only 28% of the pixels. In agreement with our results, Garonna et al.<sup>37</sup> showed that the GSL increased significantly from 1982 and 2011 only over 18–30% of the European land area. It seems that including more recent years in analysis diminishes the lengthening trend in GSL and the percentage of the land surface over which it occurs, indicating that the trend has changed more recently. Based on Supplementary Fig. 3a showing the spatial patterns of the long-term (1982–2020) trend slope of GSL data, central Europe mainly shows positive trends for GSL with trend slopes varying between 0 to 1 d/y while the lower latitudes along with higher latitudes show a decreasing trend in GSL data (see Supplementary Fig. 3b, c to find out about the spatial patterns of OG and OD).

As part of a periodic trend analysis, we examined whether the trend slope of GSL (as well as OG and OD) varied across the

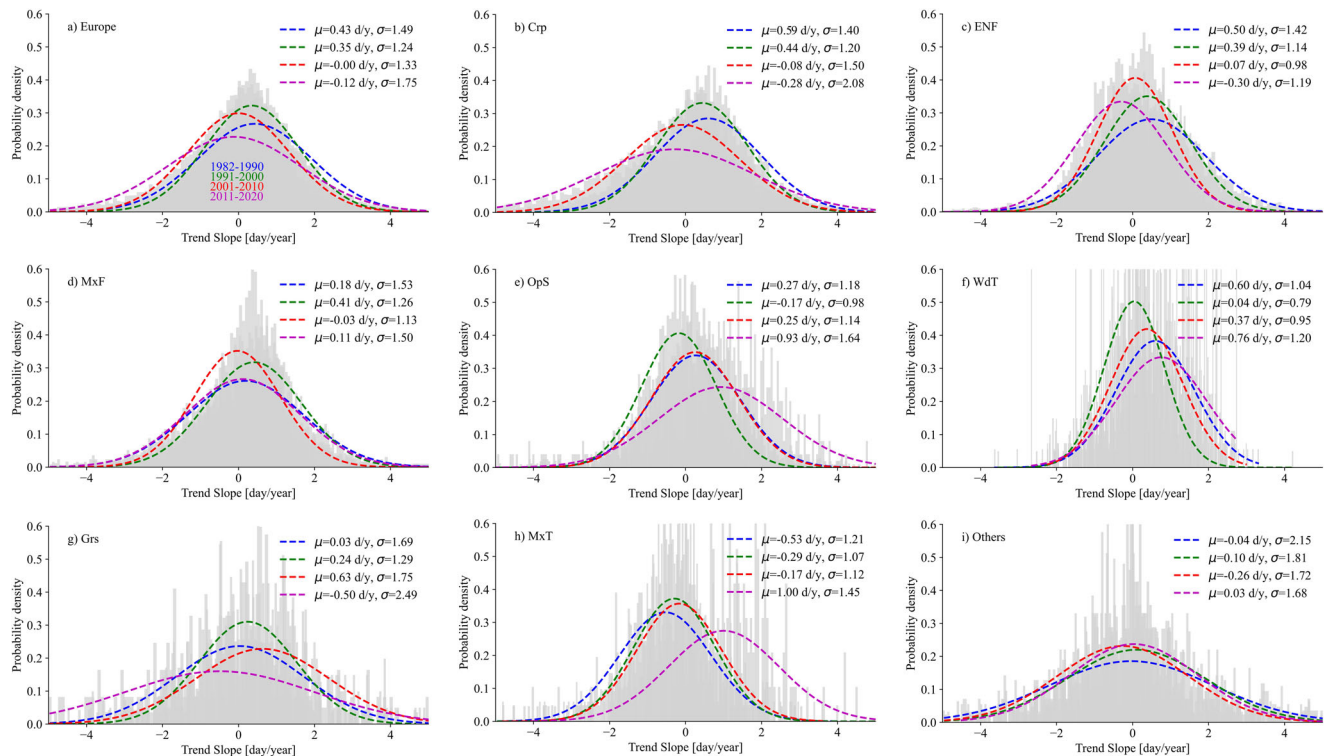


**Fig. 5 Histograms and probability distribution functions (PDFs) of changes in length of growing season for different decades under different land cover types.** The changes are quantified by trend parameter from Mann-Kendall analysis. Panel **a** shows the histograms (grey bars) and PDFs (dashed lines) for entire Europe, panel **b** for croplands (Crp), panel **c** for evergreen needleleaf forests (ENF), panel **d** for mixed forest (MxF), panel **e** for open shrublands (OpS), panel **f** for wooden tundra (WdT), panel **g** for grasslands (Grs), and panel **i** for mixed tundra (MdT). The letter  $\mu$  and  $\sigma$  correspond to the mean and standard deviations.

1982–1990, 1991–2000, 2001–2010, and 2011–2020 time periods. Interestingly, Europe shows a positive mean GSL trend slope of 0.43 and 0.35 d/y for the first and second periods, respectively. These imply nearly one week longer growing seasons at the end of the second period (Fig. 5). The trend then drops to zero for the third decade (2001–2010), with a tendency toward negative values. During the past decade (2011–2020), however, the trend changes to negative, with a mean trend slope of  $-0.12$  d/y, which offsets almost one-third of the earlier GSL shift of the first decade. A similar behavior (positive trends of GSL in the first two periods and negative trend in the last decades) is observed in croplands, evergreen needle leaf forests, and grasslands. However, it appears that for wooden tundra, mixed forests, and open shrublands the lengthening trend in GSL is continuing except for open shrublands. The mixed tundra is also an exception, where we see a positive trend in the last period (2011–2020) and negative trends in the remaining periods. Excluding open shrublands and tundras, the strongest negative trend in the last period is observed in grasslands with a rate of  $-0.50$  d/y, followed by croplands and evergreen needleleaf forests with a rate of  $-0.29 \pm 0.01$  d/y. A pessimistic projection of these results could therefore lead to the conclusion that we face a further decrease in GSL in most vegetation types in Europe after 2020, due to severe dry and warm years that occurred since then.

While Europe has experienced an average OD trend of  $-0.31$  d/y over the last period (2011–2020), there also has been a reduced shift in OG with a trend slope of  $-0.19$  d/y (see Supplementary Figs. 4 and 5). Combined, these reverse the trend of GSL over the last period and offsets the lengthening of GSL in previous periods. However, to determine when such a reversal in trend of GSL (and OG and OD) occurs, we did another trend analysis, this time setting the data period to a 15-year moving window and

relocating the window over different years from 1982–2020. We think in this way we were able to see which year is critical and at what point the reversal occurs. The results (Fig. 6) show that the reversal in GSL trend occurs after 2003–2004, probably due to the severe drought we had in Europe in 2003. However, we still see a positive trend for GSL till 2013–2014, meaning that the growing season is still lengthening, albeit at a slower rate. However, after 2014, the trend gets negative meaning that the season length is shortening.

Subsequently, we determined control factors (see Supplementary Figs. 6–8) for anomalies ( $\Delta$ ) in OG and OD as well as GSL using the GMDH<sup>38</sup> framework (see Methods) together with main meteorological variables (T, P, and VPD) as well as surface SM (SSM) and root zone SM (RSM) from GLDAS-NOAH<sup>39–41</sup>, ERA5-Land<sup>42</sup>, and GLEAM<sup>43,44</sup> databases. All variables are averaged for winter [January 1 until 30 days before OG], early spring [30 days before OG to OG], spring [OG to the peak of greening, PG], summer [PG up to two weeks before OD], and late summer [two weeks before OD to OD] times. We performed a pixel-wise analysis of control factors and aggregated the results for groups of pixels corresponding to their dominant land use.

Our analysis shows that  $\Delta T$  and  $\Delta VPD$  in late summer beside  $\Delta T$  in early spring and spring are the most important control factors for GSL (Supplementary Fig. 6). For almost 28% of the pixels, late summer  $\Delta T$  is the first important factor entering the model. For nearly 13% of the remaining pixels, it is also important as a second control factor. Similarly,  $\Delta T$  in early spring is the first and second important factor entering the model for nearly 12 and 8% of the pixels, respectively. Overall, for almost 54% of the pixels,  $\Delta T$  (either in spring or summer) is the most important factor for GSL. For 40% of the remaining pixels,  $\Delta T$  is still the second most important factor for GSL.



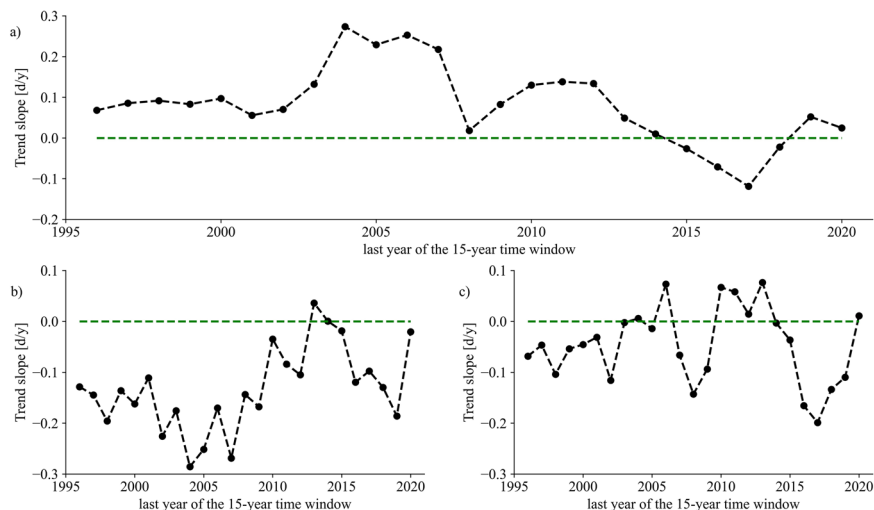


**Fig. 6** Variation of average trends of length, beginning, and end of European growing seasons during 1982–2020. Panel **a** shows the length of growing season, panel **b** onset of greening, and panel **c** onset of dormancy. Trends are analyzed by applying a moving time window of 15-years from 1982–2020.

$\Delta$ VPD in late summer is the second important variable for the model. For almost 16% of pixels,  $\Delta$ VPD in late summer is the most important control factor of GSL, while for 10% of pixels it is the second most important control factor. Regardless of the period for which an average is taken,  $\Delta$ VPD is the first and second important control factor for GSL for nearly 29 and 22% of pixels, respectively. Finally,  $\Delta$ P is the third most important variable controlling GSL, being the first control factor for almost 10% of pixels and the second for 15%.  $\Delta$ SM (both at the surface and in the root zone) clearly has the least influence on GSL. Looking at the control factors for OG and OD, we found that  $\Delta$ T and  $\Delta$ VPD in early spring are the most important control factors for OG (see Supplementary Fig. 7a) and  $\Delta$ T in late summer and summer along with  $\Delta$ VPD in late summer are the most important control factors for OD (see Supplementary Fig. 7b). This means that the availability of SM to plants is the least limiting factor for plant growth in Europe, even though climate change has probably altered P patterns in Europe. This shows that, in contrast to other publications<sup>20</sup> citing SM deficit (especially in summer) as the most important factor driving changes in OD, at least SM availability has not played such a prominent role in Europe until 2020. This conclusion raises the question: if SM is less of a constraint, why did we still observe a shortening of GSL during recent years, even though OG still shifted to earlier dates, albeit at a slower rate? A possible answer is that AWD was increased due to warmer conditions (reflected in increased average T and VPD), and water supply was therefore below plant water demand (caused by higher AWD), which led to earlier OD. A principal component analysis (PCA) between OG and other variables (Supplementary Fig. 9a) showed that OG is negatively correlated with T, VPD and P in winter and early spring, while other variables, including SSM and RSM, are not correlated with OG. This means that the higher the T, VPD, and P are in winter and early spring, the earlier OG is reached. In a similar analysis (Supplementary Fig. 9b), OD shows a negative correlation with VPD and T in summer and late summer and a positive correlation with P in all periods, i.e., the higher the VPD and T are in summer and late summer, the earlier OD is reached or the higher the P, the later the OD is reached. As mentioned earlier, there is no significant correlation between OD and other variables, especially SSM and RSM.

We also examined the spatial distribution of the main control factors of OG (Fig. 7) and OD (Fig. 8). To facilitate interpretation, we did not distinguish the variables by the period for which an

average is taken. As shown in Fig. 7, T, VPD, and P are the main triggers of early greening across Europe, with VPD more prominent in coastal areas with latitude less than 60 degrees, P mainly in central Europe, and T in the remaining areas. The second most dominant control factor was more difficult to determine. However, T and P and to some extent RSM still play a role here. In the case of early dormancy, the message is clearer, as T, VPD, and to some extent P can be identified as major triggers of early dormancy in Europe. Inspection of the second dominant controlling factor of OD (Fig. 8) also clearly shows that SSM and RSM control OD less strongly.

Different reasons can be invoked to explain the observed behavior for different land use types. In general, Europe-wide trends in OG are driven to a large extent by the pattern observed for wooden and mixed tundra (Supplementary Fig. 4). These high-latitude ecosystems are very sensitive to climate change, so a small increase in temperature has a greater impact there than in temperate regions<sup>45</sup>. This likely explains why early spring T the most important controlling factor for the OG (Supplementary Fig. 7a) is and, consequently, one of the two most important variables in explaining GSL. Similarly, the earlier OD is primarily due to cropland and grassland, which are generally expected to have shallower root systems than the other woody land-use classes. It is therefore not surprising that late summer T and VPD were the most important and second most important environmental variables for these types of land uses. This is because grasses and cropland are sensitive to drought (without consideration of possible irrigation) and easily sense or complete their life cycle toward early harvesting, thus shortening their apparent GSL. Earlier harvest, especially for croplands, can have several implications, both positive and negative, depending on the specific crop, the timing and frequency of harvest, and local environmental conditions. However, due to the coarser resolution of the data used in this analysis (0.25 degrees), it was not possible to examine harvest timing for cropland. This may require a more detailed examination of the croplands to account for the appropriate conditions. However, to determine if our expectation was generally true for cropland and grassland, we examined the control factor of GSL (as well as OG and OD) in different land use types (results not shown). In the case of GSL, almost the same factors as Europe play a role within the different vegetation types, except for tundra (both wooden and mixed) and to some extent for evergreen needle leaf forests. For evergreen needle leaf forests, the only difference compared to other land use types is that late

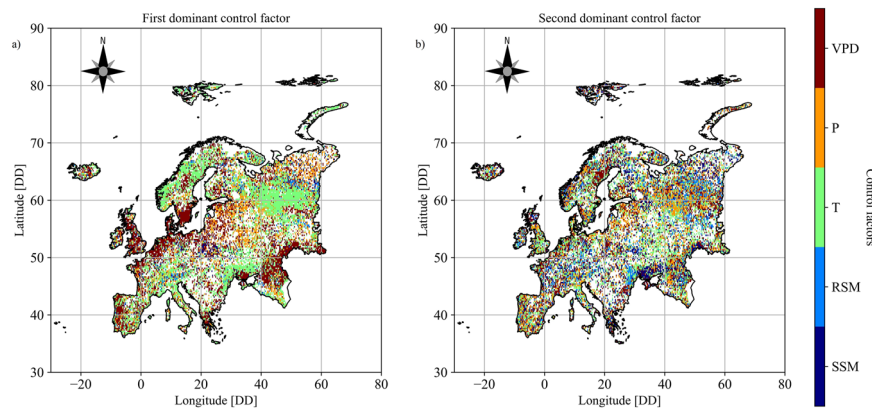


**Fig. 7** The spatial distribution of the control factors for the onset of greening in Europe. Panel **a** shows the spatial distribution for the first control factor and panel **b** for the second control factor. SSM and RSM refer to surface soil moisture and root zone soil moisture, respectively, T is temperature, P precipitation, and VPD vapor pressure deficit.

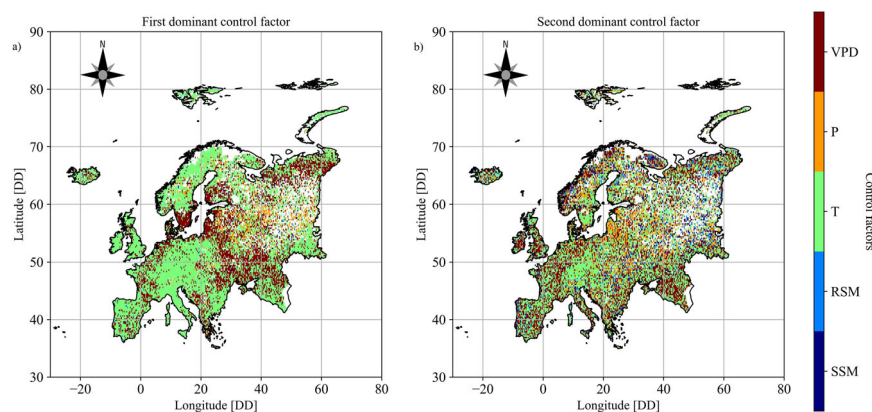


**Fig. 8** The spatial distribution of the control factors for the onset of dormancy in Europe. Panel **a** shows the spatial distribution for the first control factor and panel **b** for the second control factor. SSM and RSM refer to surface soil moisture and root zone soil moisture, respectively, T is temperature, P precipitation, and VPD vapor pressure deficit.

summer  $\Delta$ VPD plays a lesser role and dominates 14% of the pixels of this land cover, compared to 26% in Europe. For mixed and wooden tundras, the importance of late summer variables for GSL decreases even more. The other dominant land cover types in Europe, including croplands, mixed forests, grasslands, and open shrublands, show almost the same behavior as we observed for Europe as a whole. Almost the same results were also obtained for OD and OG (not shown).

To support the results of the GMDH analysis, we performed an additional trend analysis over late summer ET, RSM, SSM, T, VPD, and P data. Results show no significant trend for SSM, RSM, P, and ET, but significant increasing trends for T and VPD in most pixels in Europe, which is consistent with our previous reports. This is confirmed by both reanalysis (see Supplementary Table 1) and in situ data (Supplementary Fig. 10). Supplementary Discussion 2 also provides some additional information on this topic.

The ecohydrological feedback we highlighted in our research (onset of wilting/senescence at higher SM when ET is higher) is already well documented. For example, in one of the first studies on the relationship between ET and SM, Brown<sup>46</sup> experimentally showed 110 years ago that the transpiration rate affects the SM threshold at which wilting occurs. If the transpiration rate is high, plants will wilt at a higher SM, while at a lower transpiration, plants will gradually be able to absorb more water from the soil, so that wilting will occur only when the SM is lower. Gao et al.<sup>47</sup> also noted that OD occurs earlier despite still having sufficient SM, but plant's root systems are adapted to extracting the amount

of water that is normally required and that amount changes probably due to increased VPD.

Our results implicate that changes in OG and OD and consequently in GSL will directly affect the net carbon balance of the ecosystem<sup>48–50</sup>, the exchange of water and energy with the atmosphere<sup>51</sup> and management of ecosystems but the impact of these changes is not yet accounted for in land surface models. To cope with these changes agricultural management practices will need to be adapted in terms of suitable crop selection and breeding (e.g., optimally designed root systems), crop rotation and intercropping (e.g., avoiding bare soil) and irrigation management to optimally exploit the change in GSL.

## Methods

**Study area and working units.** This study is conducted at the scale of the European continent (Supplementary Fig. 11). We classified all pixels within Europe using the GLDAS Vegetation Class/Mask<sup>40</sup> (see Supplementary Fig. 11). To classify the pixels, dominant GVC land cover types were selected for further analysis. Selected land cover types include croplands, evergreen needleleaf forests, mixed forests, open shrublands, wooden tundra, grasslands, and mixed tundra. Once the work units were identified, all calculations were performed on a pixel-by-pixel basis and then the results within each work unit were averaged (wherever necessary) to obtain class-specific results.

**Datasets.** Data from different sources are used for this analysis. We used NDVI (Normalized Difference Vegetation Index) data from the Global Inventory Monitoring and Modelling System (GIMMS)<sup>26,27</sup> (covering the period 1981–2015), the Advanced Very High-Resolution Radiometer (AVHRR)<sup>28</sup> (covering the period 1981–2020), and the Moderate Resolution Imaging Spectroradiometer (MODIS)<sup>29</sup>

(covering the period 2001–2020) to determine OG and OD and consequently GSL. In addition, the NASA Global Land Data Assimilation System (GLDAS) along with the NOAA Land Surface Model<sup>40,41</sup> (v2.0<sup>52</sup>, for 1982–2014, and v2.1<sup>39</sup>, for 2000–2020), the European Centre for Medium-Range Weather Forecasts (ECMWF) ERA5-land<sup>42</sup> (for 1982–2020), and the Global Land Evaporation Amsterdam Model<sup>43,44</sup> (GLEAM v3.6a, for 1982–2020) were the three other datasets used in this analysis. We also used in situ measurement data from FLUXNET<sup>53</sup> (with a duration of 1995–2020) as a benchmark for the reanalysis data used.

**Data preprocessing.** The data used in this analysis from different sources are provided at different spatial resolutions, with the coarser resolution being 0.25 degrees for GLDAS and GLEAM databases. Therefore, for consistency, we used the Regular-GridInterpolator function of the interpolate sub-package of the Python package of scipy to aggregate them (wherever necessary) with a resolution of 0.25 degrees, using the same latitude and longitude vectors of the GLDAS and GLEAM databases. Since this aggregation could smooth the data, we performed a statistical analysis to ensure the accuracy of the aggregated data. In the absence of ground truth data, we compared the standard deviation of the original and aggregated data to determine their smoothness showing that the reduction in standard deviation of the aggregated data compared to the original data is less than 5% on average, which seems to be fine. In addition, we compared the original and aggregated maps using a moving squares method. To do this, we placed a  $2.5 \times 2.5$ -degree squared quadrat over both maps and averaged the data within the square for both maps. We then moved the square across the maps in 2.5 degree increments and averaged the data for both maps. Finally, we had two vectors of equal size for averaged data. We then calculated the Nash-Sutcliffe criterion (E) between these averaged data. The E showed a value above 0.95, indicating a very strong correlation between the original and aggregated values. Therefore, we expect that these aggregation steps introduce less uncertainty into our analysis.

In the case of the NDVI data, we used the GIMMS NDVI data as a benchmark for our analysis because it is commonly used in other studies. However, it should be noted that the GIMMS NDVI data are available at biweekly temporal resolution (i.e., two data per month), the MODIS NDVI data are available at monthly resolution, and the AVHRR NDVI data are available at daily resolution. Therefore, we brought them all to monthly resolution by averaging the data that fall within each month, i.e., in the case of the GIMMS data, the two data within each month, and in the case of the AVHRR data, all daily data of each month. This was necessary because the temporal resolution of the NDVI data affects the derived OG and OD values. Additionally, we excluded the last three years of AVHRR data (2018–2020) from the analysis due to unknown quality of the data for these years.

The Princeton meteorological forcing data used for GLDAS 2.0 ends in 2014, so GLDAS 2.1 (covering 2001–present) uses other forcing data including observation-based P and solar radiation, resulting in significantly higher values nearly for all variables, as the climatology of the forcing variables differs from that of the Princeton forcing dataset. Therefore, we used the overlapping period 2001–2014 to construct location- and day of year-specific linear regressions between paired variables from v2.0 and v2.1, and then applied the developed regressions to match the GLDAS 2.1 data to the climatology of 2.0. In the case of P, day of year-specific linear regressions were not possible due to high variability and frequency of zero values, therefore we only applied site-specific linear regressions.

While the temporal resolution of the GLEAM dataset is daily, the GLDAS data are provided with a temporal resolution of 3 h. Therefore, we averaged the 3-hourly data from GLDAS to account for the daily data. Although the ERA5-Land dataset is originally provided with a spatial resolution of 0.05 degrees and a temporal resolution of 1 h, for consistency, we downloaded the daily and 0.25-degree resolution data using the ERA5-Land Daily Statistics CDS API (<https://cds.climate.copernicus.eu/cdsapp#!/software/app-c3s-daily-era5-statistics>).

In cases where a variable was available from two or more of the above reanalysis products, a PCA was performed, and the first component was then used for further analyses when the target variable was in demand. This was the case for ET and SSM. In the case of ET, the first component accounted for 95 or more percent of the variation in all products, while in the case of SSM, 85 or more percent of the variation in the products used was explained by the first component.

**Data validation.** Before any further analysis, we validated ET and SSM data from the datasets used (GLDAS, GLEAM and ERA5-Land) by comparing them with in situ measurement data from FLUXNET<sup>53</sup>. For this purpose, we extracted reanalysis data on ET and SSM for the pixels containing FLUXNET stations for the overlapping periods 2000–2020, and then performed a station-by-station comparison of the reanalysis data with the FLUXNET data. In total, 8 and 23 FLUXNET stations contain the complete data for ET from all datasets for the 2000–2009 and 2010–2020 periods, respectively, while only 4 and 18 stations have the complete data for SSM from all datasets for the 2000–2009 and 2010–2020 periods, respectively. Supplementary Fig. 12 shows the Pearson correlations between ET and SSM from FLUXNET and ET and SM from other datasets. There are strong correlations between ET from FLUXNET and ET from GLDAS, GLEAM and ERA5-Land with correlation coefficients ranging from 0.59 to 0.87 for the period 2000–2009 and 0.64 to 0.91 for the period 2010–2020. In contrast to ET, the correlations between SSM from FLUXNET and SSM from GLDAS, GLEAM and ERA5-Land appear to be weak (with correlation coefficients ranging from 0.24 to 0.60 for the period 2000–2009 and 0.07

to 0.83 for the period 2010–2020), partly due to uncertainty of SSM measurements at FLUXNET stations, as seen in the large changes in SSM values or repeated constant values for some months. Overall, it seems that the reanalysis data used in this investigation can reasonably show the ongoing trend in the real world, and we can be confident that the conclusions we have drawn in this paper are valid.

**LFD NDVI method.** To determine OG and OD for individual pixels in Europe and for individual years of the entire study period (1982–2020), we needed an innovative algorithm that could operate independently for each year and pixel. This was important because classical methods, e.g., Piao et al.<sup>54</sup>, typically calculate a critical long-term NDVI value for the entire period and then determine the timing for approaching such a critical value in all individual years. However, this was prone to bias because the NDVI data used came from three different products of GIMMS [1982–2015], AVHRR [1982–2017], and MODIS [2001–2020], especially with different temporal resolutions (biweekly, daily, and monthly), which can affect the long-term critical value and consequently the timing for OG and OD. Therefore, we developed the logistic function derivative of NDVI (LFD-NDVI) curve method to determine OG and OD. It uses the first and second derivatives of the fitted logistic function of the cumulative NDVI curve to determine OG and OD (Fig. 9a). As a first step, we converted all data to a monthly time scale, as mentioned earlier. Then we calculated the cumulative NDVI data over time and finally fed them into the LFD-NDVI method to determine OG and OD. However, before feeding the data into the LFD-NDVI method, we normalized both the NDVI and time data between 0 (min) and 1 (max) as this was required for further calculation. Normalization of the NDVI data was done twice, once before accumulation to eliminate possible negative NDVI values, and another time after accumulation to bring them within the range of 0 to 1. In the following, the calculation with the LFD-NDVI method is described in detail.

In a first step, a logistic function was fitted to the data (Fig. 9b):

$$y(t) = a + \frac{b}{1 + \exp(-\frac{t-c}{d})} \quad (1)$$

where  $y(t)$  is the rescaled cumulative NDVI on day  $t$  of the year,  $t$  is the rescaled time (day of the year), and the model coefficients are  $a$ ,  $b$ ,  $c$ , and  $d$ . Using this fitted function, we obtained the smoothed curve of the rescaled cumulative NDVI data for all days of the year ( $t = 1:365$  or  $366$ , being scaled to 0 and 1). Third, we determined the curvature of the data,  $k(t)$ , for each  $t$  using the first  $y'(t)$  and second  $y''(t)$  derivatives of the fitted logistic function:

$$k(t) = \frac{|y''(t)|}{(1 + y'(t))^{1.5}} \quad (2)$$

Plotting  $k(t)$  versus  $t$  typically show two maxima separated by a minimum. The times at which the maxima occur allow the logistic curve to be divided into three parts with nearly linear behavior (Fig. 9c). The first part occurs during the winter and early spring before the first curvature maximum in the data; we refer to this part as winter dormant period. The second part occurs between the first and second curvature maxima in the data; we refer to this part as active growth period. Finally, the third part occurs during the late summer and falls after the second curvature maximum in the data; we refer to this part as fall dormant period.

For the second part, a first-order polynomial function was fitted by simply using two points of maximum curvature and their respective rescaled cumulative NDVI values, plus an additional point in between. However, we used the sequential linear approximation method described by Dathe et al.<sup>55</sup> to identify the linear part of the rescaled cumulative NDVI curve before the first and after the second curvature maxima. The method consists in calculating linear regressions over a consecutive number of points before the first and after the second curvature maximum. The dependence of  $R^2$  on the number of data points was used to determine the number of points to be included in the regression. In this analysis, an  $R^2$  value of 0.95 was used as the critical value to determine the linear parts of winter- and fall-dormant. When such an  $R^2$  value was not obtained from a larger number of data, we simply used the first and last three points to draw the line in the winter- and fall-dormant periods. Next, we determined the equation of the bisector of the obtuse angle between the regression equations of the winter-dormant and active growth parts (Eq. (3)) and the fall-dormant and active growth parts (Eq. (4)) by computing the angle between two lines.

$$y(t) = a_{wa}t + c_{wa} \quad (3)$$

$$y(t) = a_{fa}t + c_{fa} \quad (4)$$

where  $a_{wa}$  and  $c_{wa}$  correspond to the slope and intercept of the line bisecting the lines of winter dormancy and active growth parts, and  $a_{fa}$  and  $c_{fa}$  correspond to the slope and intercept of the line bisecting the lines of fall dormancy and active growth parts. After determining the equations for the bisecting lines, the intersection between them and the fitted logistic function determines OG and/or OD (Fig. 9d). Mathematically, OG and OD are calculated by solving following equations for  $t$ :

$$a_{wa}t + c_{wa} = a + \frac{b}{1 + \exp(-\frac{t-c}{d})} \quad (5)$$

$$a_{fa}t + c_{fa} = a + \frac{b}{1 + \exp(-\frac{t-c}{d})} \quad (6)$$



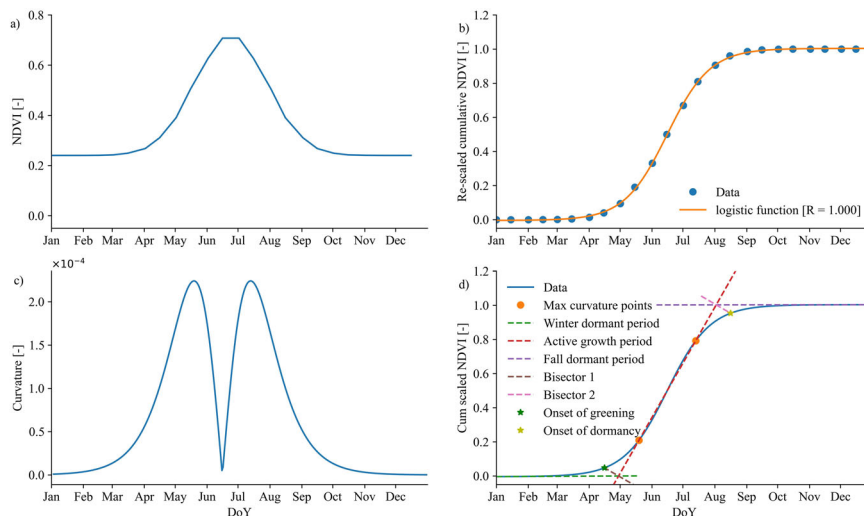


**Fig. 9** An illustrative example of the application of the LFD-NDVI method to determine the onset of greening and dormancy. Panel **a** shows the variation of NDVI over different days of the year, panel **b** shows the rescaled cumulative NDVI curve over different days of the year, panel **c** shows the variation of the curvature of the NDVI curve during different days of the year, and panel **d** graphically shows the calculation steps of the LFD-NDVI method for determining the onsets of greening and dormancy. DoY refers to the day of the year, although we have used the names of the months for illustrative purposes. In addition, for calculation purposes, DoY needs to be scaled to 0 and 1.

**Table 1** Scaling factors for the onset of greening and the onset of dormancy obtained from MODIS and AVHRR products and comparison with those obtained from GIMMS data.

Land use types	$\alpha_y$ (mean $\pm$ STD)		$\beta_y$ (mean $\pm$ STD)	
	MODIS	AVHRR	MODIS	AVHRR
Cropland	0.953 $\pm$ 0.024	0.551 $\pm$ 0.019	0.96 $\pm$ 0.012	0.826 $\pm$ 0.011
Evergreen Needleleaf Forest	1.021 $\pm$ 0.016	0.597 $\pm$ 0.018	0.959 $\pm$ 0.010	0.841 $\pm$ 0.011
Mixed Forest	0.976 $\pm$ 0.018	0.581 $\pm$ 0.019	0.958 $\pm$ 0.010	0.835 $\pm$ 0.011
Open Shrublands	0.955 $\pm$ 0.038	0.575 $\pm$ 0.012	1.003 $\pm$ 0.014	0.853 $\pm$ 0.017
Wooded Tundra	0.962 $\pm$ 0.137	0.605 $\pm$ 0.016	1.000 $\pm$ 0.022	0.866 $\pm$ 0.020
Grassland	1.028 $\pm$ 0.045	0.533 $\pm$ 0.027	0.979 $\pm$ 0.033	0.808 $\pm$ 0.021
Mixed Tundra	0.970 $\pm$ 0.051	0.615 $\pm$ 0.019	0.991 $\pm$ 0.015	0.871 $\pm$ 0.013
Others	0.833 $\pm$ 0.036	0.523 $\pm$ 0.040	0.963 $\pm$ 0.015	0.828 $\pm$ 0.024

In this analysis, the `root_scalar` function of the `Optimize` sub-package of the Python package of `scipy` (as an alternative to the “`fzero`” function in MATLAB) was used to find a null of the above expression by changing the  $t$  values.

Using the above-mentioned method, we determined OG and OD from three different NDVI products of the GIMMS (for the period 1982–2015), the AVHRR (for the period 1982–2017), and the MODIS (for the period 2001–2020). Applying a scaling approach, we corrected OG and OD data from MODIS and AVHRR to the GIMMS OG and OD data. The higher quality of GIMMS data is already well documented in literature justifying its use as benchmark<sup>25,56,57</sup>. In this scaling approach, we considered different land use levels to adjust the OG and OD results of the AVHRR and MODIS to GIMMS. In a first step, pixels of common land use types were identified, and two linear equations were defined:

$$OG_y^{GIMMS} = \alpha_y \times OG_y^i \tag{7}$$

$$OD_y^{GIMMS} = \beta_y \times OD_y^i \tag{8}$$

where  $i$  stands for MODIS or AVHRR and  $y$  stands for an individual year falling into the common periods of each pair. These equations were fitted to the GIMMS-MODIS and GIMMS-AVHRR pairs. The common period is 2001–2015 in the case of GIMMS-MODIS pair and 1982–2015 in the case of GIMMS-AVHRR pair. Then, the average of the yearly estimated scale parameters  $\alpha_y$  and  $\beta_y$  were applied on OG and OD data obtained from MODIS and AVHRR. After scaling OG and OD data from MODIS and AVHRR, the averaged values for OG and OD values from all three products were used for further analysis. The following Table provides obtained scaling factors for both OG and OD values obtained from MODIS and AVHRR products (Table 1).

We conducted no comparison between OG and OD dates obtained from our analysis and in-situ measurements because:

1. The scale mismatch between the pixel size of the space-based NDVI and in situ phenological databases such as Pan-European Phenology<sup>58</sup> or PhenoCam Dataset<sup>59</sup> prevents us from making such a comparison, since our analysis is performed at 0.25 degrees (~25 km), whereas Pan-European Phenology provides phenological data at 10 m resolution for various tree and plant species, and PhenoCam Dataset provides a time series of vegetation phenological observations (digital camera images) for 393 sites in different ecosystems around the world by main focus in North America.
2. A comparison of phenological data derived from the PhenoCam dataset and satellite remote sensing data (e.g., MODIS data at 500 m resolution, which can be considered high resolution compared to our data at ~25 km) has already been performed (e.g., Richardson et al.<sup>60</sup>), which showed high overall agreement between phenological data from in situ measurements and MODIS NDVI with an R value of 0.81, although the agreement was poor for evergreen needleleaf forests due to their minor seasonal dynamics. Therefore, we caution that our results and discussions may be uncertain wherever evergreen needleleaf forests are involved.
3. In respect to the LFD-NDVI method, we note that all methods used to derive OG and OD from NDVI curve assume that bud break for a given pixel occurs at a specific NDVI threshold that is greater than the observed NDVI minimum value in winter and early spring. For example, OG is commonly defined as the day of the year when NDVI reaches the NDVI minimum plus 20% of the NDVI range<sup>61–64</sup> or the critical NDVI value determined from long-term average annual curve of NDVI<sup>16</sup>. The same also applies for OD. In our work, however, we determined this critical NDVI value by cumulatively plotting NDVI. This allowed us to show that the curve consisted of three parts that could be approximated linearly and that correspond to different growing periods. The critical NDVI values were then determined by calculating the intersection of the bisectors of the first two (in the case of OG) or last two (in the case of OD) lines and the cumulative

curve rather than an arbitrary criterion of minimum NDVI plus 20% of the NDVI range or long-term average critical NDVI. Any remaining uncertainties in our OD and OG estimates are therefore systematic and should not affect our trend analysis.

**Trend analysis of Mann-Kendall test.** In this analysis, we examined the overall trend of OG and OD as well as GSL using the Mann-Kendall test<sup>30,31</sup>. To do this, we applied the Python implementation of the nonparametric Mann-Kendall trend analysis called `pyMannkendall`<sup>65</sup> employing the original and Theil-Sen methods with a significance level of 0.05. Both original and Theil-Sen methods show how OG, OD, and/or GSL change with time, but Theil-Sen is more robust against individual outliers<sup>66</sup>. As suggested by Cortés et al.<sup>66</sup>, prior to trend analysis, we dealt with temporal autocorrelation of data with AR(1) correction to prevent the occurrence of false positive rates<sup>67</sup>. As suggested by von Storch<sup>67</sup> and outlined by Cortés et al.<sup>66</sup>, the following equation is used to calculate the temporal autocorrelations at lag -1:

$$\hat{r} = \frac{n \sum_{t=1}^{n-1} (x_t - \bar{x})(x_{t+1} - \bar{x})}{(n-1) \sum_{t=1}^n (x_t - \bar{x})^2} \quad (9)$$

where  $\hat{r}$  is autocorrelation,  $x_t$  is data at time  $t$ ,  $\bar{x}$  is the mean value of all data, and  $n$  is number of the data. Then, when autocorrelation is computed, the original time series ( $x_t$ ) were replaced with adjusted one ( $y_t$ ) using following equation:

$$y_t = x_t - \hat{r}x_{t-1} \quad (10)$$

**Group method of data handling.** We applied the group method of data handling (GMDH)<sup>38</sup> pixel-wisely to develop a gray box network predicting OG and OD, and GSL, using several meteorological variables along with soil moisture as inputs. For this purpose, we examined the factors that affect energy and water supply for transpiration as one of the main functions of green vegetation under changing climatic conditions. Therefore, we chose the meteorological variables T, P, and VPD because we believe that T and P directly reflect the effects of changing climate on transpiration and VPD combines the effects of all major weather parameters that affect transpiration (e.g., radiation, air temperature, humidity, and wind speed)<sup>68,69</sup>. In other words, these are the main meteorological variables that affect both energy and water supplies and can better express changing climatic conditions. In addition, we also used SSM and RSM because they are direct state variables for water availability to vegetation. We excluded ET and transpiration from this analysis because they, as main function of the green vegetation, are logically strongly correlated with the phenological states of vegetation and mask the importance of other variables. We also excluded climate indices (NAO: North Atlantic Oscillation, El Nino, etc.) from this analysis because the pretest showed that in this context, they play a lesser role than the other included variables. All included variables were averaged for several time periods, namely winter [January 1–30 days before OG], early spring [30 days before OG to OG], spring [OG to PG], summer [PG to the 14 days before OD], and late summer [14 days before OD to OD]. Then, their long-term anomalies were calculated for each period and then subjected to modeling.

The following quadratic regression is used to obtain the preliminary estimates ( $z_{ij}$ ) for the first layer of the GMDH network<sup>70</sup>:

$$z_{ij} = c_0 + c_1x_i + c_2x_j + c_3x_i^2 + c_4x_j^2 + c_5x_ix_j \quad (11)$$

where  $x_i$  and  $x_j$  represent the pairwise selection of input variables and  $c_0$  to  $c_5$  represent the polynomial predictors. The following equation determines the total number ( $n$ ) of possible polynomials<sup>70</sup>:

$$n = \frac{N \times (N - 1)}{2} \quad (12)$$

where  $N$  is the number of input variables. To develop the GMDH network, we first developed all possible polynomials with pairwise selected variables ( $x_i$  and  $x_j$ ). Then we had to filter out the least effective new variables using a statistical selection criterion<sup>38</sup>. We used the following criteria to select the best new variables to build the next layer of the network<sup>71</sup>:

$$e = p \times RMSE_{\text{lowest}} + (1 - p) \times RMSE_{\text{highest}} \quad (13)$$

where  $p$  is the selection pressure and means a number between 0 and 1 (with  $p = 0.75$  in our analysis), with higher numbers indicating higher pressure in selecting new variables. The preliminary estimates with root mean square error (RMSE) smaller than  $e$  were selected for the next layer. The polynomials were then further improved by repeating steps 1 and 2 and using the selected variables ( $z_{ij}$ ) from the previous step. This continues until the smallest value of the selection criterion from the current iteration shows no improvement over the smallest value from the previous iteration<sup>70</sup>.

To develop GMDH models for predicting anomalies in GSL (the same applies for OG and OD), we forced the models to have only one layer with two most important variables going into the model. The concept underlying this strategy is to select only two variables for each pixel for predicting OG and OD or GSL. To train and evaluate the developed networks, the data were randomly split into two

subsets, with 70 percent of the data used to train the networks and the rest used to test as independent data.

The GMDH method provides a built-in algorithm<sup>70,71</sup> that retains only the essential input variables. Therefore, here we repeated 100 times the random division of the data into training and test subsets and calculated the Pearson correlation ( $R$ ) between the target and output variables for each replication. Then, the replications with  $R$  value less than 0.7 in the evaluation subset were filtered out and the selected sets of variables for predicting the onset of the OG and OD and GSL in the remaining replications were determined. The used GMDH algorithm is coded in Python.

To visualize the results obtained from GMDH analysis, the first and second important control factors of anomalies of GSL (as well as OG and OD) are plotted against each other, and the colors show their frequency among the pixels in Europe (see Supplementary Figs. 6 and 7). In this way, we were able to check which variable was the most important factor and with which other variable it usually paired to explain the anomalies in GSL (and/or OG and OD).

**Principal component analysis and biplotting.** To investigate the direction of the effects of the control factors on GSL as well as OG and OD, we performed PCA on the data and illustrated the result as biplots. Biplots show both the observations and the original variables in principal component space<sup>72</sup>. In a biplot, positively correlated variables are closely aligned, while negatively correlated variables are aligned in the opposite direction. In both cases, the stronger the correlation between variables, the larger the size of the arrows. Variables aligned at 90 degrees to each other have no correlations<sup>73</sup>.

## Data availability

Processed data can be accessed from <https://doi.org/10.5281/zenodo.7962415>. The GLDAS Vegetation Class/ Mask map is available at <https://ldas.gsfc.nasa.gov/gldas/vegetation-class-mask>. The original NDVI (Normalized Difference Vegetation Index) data from the Global Inventory Monitoring and Modelling System (GIMMS) and the Moderate Resolution Imaging Spectroradiometer (MODIS) can be accessed through direct communications with data provider (Dr. Stefan Kern from University of Hamburg, Germany). The NDVI data from Advanced Very High-Resolution Radiometer (AVHRR) is available in <https://climatedataguide.ucar.edu/climate-data/ndvi-normalized-difference-vegetation-index-noaa-avhrr>. The reanalysis data for NASA Global Land Data Assimilation System (GLDAS) is accessible from <https://ldas.gsfc.nasa.gov/gldas/gldas-get-data>. The reanalysis data of European Centre for Medium-Range Weather Forecasts (ECMWF) ERA5-Land is accessible form <https://cds.climate.copernicus.eu/>. The Global Land Evaporation Amsterdam Model (GLEAM) dataset can also be obtained from <https://www.gleam.eu/>. The in-situ measurement data from FLUXNET can be accessed from <https://fluxnet.org/>.

## Code availability

All codes are available in <https://github.com/mehdirmti/vegetation-greening-dormancy.git>.

Received: 1 November 2022; Accepted: 14 June 2023;

Published online: 03 July 2023

## References

- Zhu, K. Preliminary study on the climate change in China during last 5000 years. *Sci. China* **2**, 168–189 (1973).
- Lieth, H. in *Phenology and seasonality modeling* 3–19 (Springer, 1974).
- Schwartz, M. D. Green-wave phenology. *Nature* **394**, 839–840 (1998).
- Menzel, A. & Fabian, P. Growing season extended in Europe. *Nature* **397**, 659 (1999).
- Beaubien, E. & Freeland, H. Spring phenology trends in Alberta, Canada: links to ocean temperature. *Int. J. Biometeorol.* **44**, 53–59 (2000).
- Cleland, E. E., Chuine, I., Menzel, A., Mooney, H. A. & Schwartz, M. D. Shifting plant phenology in response to global change. *Trends Ecol. Evol.* **22**, 357–365 (2007).
- Richardson, A. D. et al. Climate change, phenology, and phenological control of vegetation feedbacks to the climate system. *Agric. Forest Meteorol.* **169**, 156–173 (2013).
- Piao, S. et al. Plant phenology and global climate change: current progresses and challenges. *Global Change Biol.* **25**, 1922–1940 (2019).
- Menzel, A. et al. European phenological response to climate change matches the warming pattern. *Global Change Biol.* **12**, 1969–1976 (2006).
- Peaucelle, M. et al. Spatial variance of spring phenology in temperate deciduous forests is constrained by background climatic conditions. *Nat. Commun.* **10**, 1–10 (2019).

11. Kern, A., Marjanović, H. & Barcza, Z. Spring vegetation green-up dynamics in Central Europe based on 20-year long MODIS NDVI data. *Agric. Forest Meteorol.* **287**, 107969 (2020).
12. Schwartz, M. D., Ahas, R. & Aasa, A. Onset of spring starting earlier across the Northern Hemisphere. *Global Change Biol.* **12**, 343–351 (2006).
13. Fu, Y. H. et al. Recent spring phenology shifts in western Europe based on multiscale observations. *Global Ecol. Biogeogr.* **23**, 1255–1263 (2014).
14. Peñuelas, J. & Filella, I. Responses to a warming world. *Science* **294**, 793–795 (2001).
15. Barichivich, J. et al. Large-scale variations in the vegetation growing season and annual cycle of atmospheric CO<sub>2</sub> at high northern latitudes from 1950 to 2011. *Global Change Biol.* **19**, 3167–3183 (2013).
16. Piao, S. et al. Leaf onset in the northern hemisphere triggered by daytime temperature. *Nat. Commun.* **6**, 1–8 (2015).
17. Liu, Q. et al. Delayed autumn phenology in the Northern Hemisphere is related to change in both climate and spring phenology. *Global Change Biol.* **22**, 3702–3711 (2016).
18. Forkel, M. et al. Codominant water control on global interannual variability and trends in land surface phenology and greenness. *Global Change Biol.* **21**, 3414–3435 (2015).
19. Keenan, T. F. & Richardson, A. D. The timing of autumn senescence is affected by the timing of spring phenology: implications for predictive models. *Global Change Biol.* **21**, 2634–2641 (2015).
20. Buermann, W. et al. Widespread seasonal compensation effects of spring warming on northern plant productivity. *Nature* **562**, 110–114 (2018).
21. Shi, C. et al. Effects of warming on chlorophyll degradation and carbohydrate accumulation of alpine herbaceous species during plant senescence on the Tibetan Plateau. *PLoS One* **9**, e107874 (2014).
22. Fracheboud, Y. et al. The control of autumn senescence in European aspen. *Plant Physiol.* **149**, 1982–1991 (2009).
23. Schwartz, M. D. *Phenology: an integrative environmental science* (Springer, 2003).
24. Hartmann, D. L. et al. in *Climate change 2013 the physical science basis: Working group I contribution to the fifth assessment report of the intergovernmental panel on climate change* 159–254 (Cambridge University Press, 2013).
25. Lian, X. et al. Summer soil drying exacerbated by earlier spring greening of northern vegetation. *Sci. Adv.* **6**, eaax0255 (2020).
26. Pinzon, J. E. & Tucker, C. J. A non-stationary 1981–2012 AVHRR NDVI3g time series. *Remote Sens.* **6**, 6929–6960 (2014).
27. NCAR in *The climate data guide: NDVI: normalized difference vegetation index-3rd generation: NASA/GFSC GIMMS* (NCAR, 2018).
28. Vermote, E. in *NOAA CDR Program, NOAA National Centers for Environmental Information* (NOAA, 2019).
29. Didan, K. in MOD13C2 MODIS/Terra Vegetation Indices Monthly L3 Global 0.05Deg CMG V061. NASA EOSDIS Land Processes DAAC. <https://doi.org/10.5067/MODIS/MOD13C2.061>; obtained from the Land Processes Distributed Active Archive Center (LP DAAC), located at the U.S. Geological Survey (USGS) Earth Resources Observation and Science (EROS) Center ([lpdaac.usgs.gov](http://lpdaac.usgs.gov)) [last access January 26, 2022], modified and converted into netCDF file format at the Integrated Climate Data Center (ICDC), CEN, University of Hamburg, Germany. (2021).
30. Mann, H. B. Nonparametric tests against trend. *Econometrica*, **13**, 245–259 (1945).
31. Kendall, M. G. Rank Correlation Methods, Griffin and Co., Ltd., London, (1948).
32. Fu, Y. H. et al. Declining global warming effects on the phenology of spring leaf unfolding. *Nature* **526**, 104–107 (2015).
33. Julien, Y. & Sobrino, J. Global land surface phenology trends from GIMMS database. *Int. J. Remote Sens.* **30**, 3495–3513 (2009).
34. Stöckli, R. & Vidale, P. L. European plant phenology and climate as seen in a 20-year AVHRR land-surface parameter dataset. *Int. J. Remote Sens.* **25**, 3303–3330 (2004).
35. Myneni, R. B., Keeling, C., Tucker, C. J., Asrar, G. & Nemani, R. R. Increased plant growth in the northern high latitudes from 1981 to 1991. *Nature* **386**, 698–702 (1997).
36. Zhu, W. et al. Extension of the growing season due to delayed autumn over mid and high latitudes in North America during 1982–2006. *Global Ecol. Biogeogr.* **21**, 260–271 (2012).
37. Garonna, I. et al. Strong contribution of autumn phenology to changes in satellite-derived growing season length estimates across Europe (1982–2011). *Global Change Biol.* **20**, 3457–3470 (2014).
38. Farlow, S. J. The GMDH algorithm of Ivakhnenko. *Am. Stat.* **35**, 210–215 (1981).
39. Beaudoin, H. & Rodell, M. NASA/GSFC/HSL, GLDAS Noah Land Surface Model L4 3 hourly 0.25 x 0.25 degree V2.1, Greenbelt, Maryland, USA, Goddard Earth Sciences Data and Information Services Center (GES DISC), Accessed: [May 27 2022], <https://doi.org/10.5067/E7TYRXPJKWOQ> (2016).
40. Rodell, M. et al. The global land data assimilation system. *Bull. Am. Meteorol. Soc.* **85**, 381–394 (2004).
41. Rodell, M. et al. NASA/NOAA's global land data assimilation system (GLDAS): recent results and future plans. In *Proceedings of the ECMWF/ELDAS Workshop on Land Surface Assimilation*. 61–68 (ECMWF, 2004).
42. Hersbach, H. et al. The ERA5 global reanalysis. *Q. J. R. Meteorol. Soc.* **146**, 1999–2049 (2020).
43. Martens, B. et al. GLEAM v3: Satellite-based land evaporation and root-zone soil moisture. *Geosci. Model Dev.* **10**, 1903–1925 (2017).
44. Miralles, D. G. et al. Global land-surface evaporation estimated from satellite-based observations. *Hydrol. Earth Syst. Sci.* **15**, 453–469 (2011).
45. Forkel, M. et al. Enhanced seasonal CO<sub>2</sub> exchange caused by amplified plant productivity in northern ecosystems. *Science* **351**, 696–699 (2016).
46. Brown, W. H. The relation of evaporation to the water content of the soil at the time of wilting. *Plant World* **15**, 121–134 (1912).
47. Gao, H. et al. Climate controls how ecosystems size the root zone storage capacity at catchment scale. *Geophys. Res. Lett.* **41**, 7916–7923 (2014).
48. Goulden, M. et al. Sensitivity of boreal forest carbon balance to soil thaw. *Science* **279**, 214–217 (1998).
49. Barr, A., Black, T. A. & McCaughey, H. in *Phenology of ecosystem processes* 3–34 (Springer, 2009).
50. Richardson, A. D. et al. Influence of spring and autumn phenological transitions on forest ecosystem productivity. *Philos. Trans. R. Soc. B* **365**, 3227–3246 (2010).
51. Peñuelas, J., Rutishauser, T. & Filella, I. Phenology feedbacks on climate change. *Science* **324**, 887–888 (2009).
52. Beaudoin, H. & Rodell, M. NASA/GSFC/HSL, GLDAS Noah Land Surface Model L4 3 hourly 0.25 x 0.25 degree V2.0, Greenbelt, Maryland, USA, Goddard Earth Sciences Data and Information Services Center (GES DISC), Accessed: [May 27 2022], <https://doi.org/10.5067/342OHQM9AK6Q>.
53. Pastorello, G. et al. The FLUXNET2015 dataset and the ONEFlux processing pipeline for eddy covariance data. *Sci. Data* **7**, 225 (2020).
54. Piao, S., Fang, J., Zhou, L., Ciais, P. & Zhu, B. Variations in satellite-derived phenology in China's temperate vegetation. *Global Change Biol.* **12**, 672–685 (2006).
55. Dathe, A., Eins, S., Niemeier, J. & Gerold, G. The surface fractal dimension of the soil–pore interface as measured by image analysis. *Geoderma* **103**, 203–229 (2001).
56. Zhou, Y. Asymmetric behavior of vegetation seasonal growth and the climatic cause: evidence from long-term NDVI dataset in northeast China. *Remote Sens.* **11**, 2107 (2019).
57. Beck, H. E. et al. Global evaluation of four AVHRR–NDVI data sets: Intercomparison and assessment against Landsat imagery. *Remote Sens. Environ.* **115**, 2547–2563 (2011).
58. Templ, B. et al. Pan European Phenological database (PEP725): a single point of access for European data. *Int. J. Biometeorol.* **62**, 1109–1113 (2018).
59. Seyednasrollah, B. et al. PhenoCam Dataset v2.0: Vegetation phenology from digital camera imagery, 2000–2018. ORNL DAAC. (2019).
60. Richardson, A. D., Hufkens, K., Milliman, T. & Frolking, S. Intercomparison of phenological transition dates derived from the PhenoCam Dataset V1.0 and MODIS satellite remote sensing. *Sci. Rep.* **8**, 5679 (2018).
61. Kang, S. et al. A regional phenology model for detecting onset of greenness in temperate mixed forests, Korea: an application of MODIS leaf area index. *Remote Sens. Environ.* **86**, 232–242 (2003).
62. Shen, M., Piao, S., Cong, N., Zhang, G. & Jassens, I. A. Precipitation impacts on vegetation spring phenology on the Tibetan Plateau. *Global Change Biol.* **21**, 3647–3656 (2015).
63. Wang, L. et al. Acceleration of global vegetation greening from combined effects of climate change and human land management. *Global Change Biol.* **24**, 5484–5499 (2018).
64. Peano, D. et al. Global variability of simulated and observed vegetation growing season. *J. Geophys. Res. Biogeosci.* **124**, 3569–3587 (2019).
65. Hussain, M. & Mahmud, I. pyMannKendall: a python package for non parametric Mann Kendall family of trend tests. *J. Open Source Software* **4**, 1556 (2019).
66. Cortés, J. et al. Where are global vegetation greening and browning trends significant? *Geophys. Res. Lett.* **48**, e2020GL091496 (2021).
67. von Storch, H. Misuses of statistical analysis in climate research. In *Analysis of climate variability* (eds von Storch, H. & Navarra, A.) 11–26 (Springer Berlin Heidelberg, 1999).
68. Allen, R. G., Pereira, L. S., Raes, D. & Smith, M. Crop evapotranspiration—Guidelines for computing crop water requirements—FAO Irrigation and drainage paper 56. *Fao* **300**, D05109 (1998).
69. Nalevanková, P., Sitková, Z., Kučera, J. & Štělčová, K. Impact of water deficit on seasonal and diurnal dynamics of European beech transpiration and time-lag effect between stand transpiration and environmental drivers. *Water* **12**, 3437 (2020).

70. Pachepsky, Y. A. & Rawls, W. Accuracy and reliability of pedotransfer functions as affected by grouping soils. *Soil Sci. Soc. Am. J.* **63**, 1748–1757 (1999).
71. Rahmati, M. Reliable and accurate point-based prediction of cumulative infiltration using soil readily available characteristics: a comparison between GMDH, ANN, and MLR. *J. Hydrol.* **551**, 81–91 (2017).
72. Gabriel, K. R. The biplot graphic display of matrices with application to principal component analysis. *Biometrika* **58**, 453–467 (1971).
73. Rahmati, M. et al. Development and analysis of the Soil Water Infiltration Global database. *Earth Syst. Sci. Data* **10**, 1237–1263 (2018).

### Acknowledgements

The authors are grateful for the guidance provided by the NASA Global Land Data Assimilation System (GLDAS) Support Team, in particular Dr. Matthew Rodell from University of Maryland, USA, and the Global Inventory Monitoring and Modeling System (GIMMS) Support Team, Dr. Stefan Kern from University of Hamburg, Germany. The authors are also grateful for the technical support provided by Horst Hardelauf, the ex-IT technician, and Dr. Andrea Schnepf at the Agrosphere Institute, IBG-3, Forschungszentrum Jülich, Germany. The comments and advice from Dr. Diego Miralles (Ghent University, Belgium) are also appreciated.

### Author contributions

M.R. and H.V. conceived this study. M.R. performed all the analyses and wrote the initial manuscript. M.R., A.G., C.P.T., W.A., W.D., H.H.F., C.M., D.O., M.S., J.V., N.E.C.V., and H.V. contributed to interpreting results, discussion, and improvement of the paper.

### Funding

Open Access funding enabled and organized by Projekt DEAL.

### Competing interests

The authors declare no competing interests.

### Additional information

**Supplementary information** The online version contains supplementary material available at <https://doi.org/10.1038/s43247-023-00890-7>.

**Correspondence** and requests for materials should be addressed to Mehdi Rahmati or Harry Vereecken.

**Peer review information** *Communications Earth & Environment* thanks Yuping Guan and the other, anonymous, reviewer(s) for their contribution to the peer review of this work. Primary Handling Editors: Olga Churakova and Aliénor Lavergne.

**Reprints and permission information** is available at <http://www.nature.com/reprints>

**Publisher's note** Springer Nature remains neutral with regard to jurisdictional claims in published maps and institutional affiliations.



**Open Access** This article is licensed under a Creative Commons Attribution 4.0 International License, which permits use, sharing, adaptation, distribution and reproduction in any medium or format, as long as you give appropriate credit to the original author(s) and the source, provide a link to the Creative Commons licence, and indicate if changes were made. The images or other third party material in this article are included in the article's Creative Commons licence, unless indicated otherwise in a credit line to the material. If material is not included in the article's Creative Commons licence and your intended use is not permitted by statutory regulation or exceeds the permitted use, you will need to obtain permission directly from the copyright holder. To view a copy of this licence, visit <http://creativecommons.org/licenses/by/4.0/>.

© The Author(s) 2023